

# NETRA: Interactive Display for Estimating Refractive Errors and Focal Range

Vitor F. Pamplona<sup>1,2</sup>

Ankit Mohan<sup>1</sup>

Manuel M. Oliveira<sup>1,2</sup>

Ramesh Raskar<sup>1</sup>

<sup>1</sup>Camera Culture Group - MIT Media Lab

<sup>2</sup>Instituto de Informática - UFRGS

<http://cameraculture.media.mit.edu/netra>

## Abstract

We introduce an interactive, portable, and inexpensive solution for estimating refractive errors in the human eye. While expensive optical devices for automatic estimation of refractive correction exist, our goal is to greatly simplify the mechanism by putting the human subject in the loop. Our solution is based on a high-resolution programmable display and combines inexpensive optical elements, interactive GUI, and computational reconstruction. The key idea is to interface a lenticular view-dependent display with the human eye in *close range* - a few millimeters apart. Via this platform, we create a new range of interactivity that is extremely sensitive to parameters of the human eye, like refractive errors, focal range, focusing speed, lens opacity, etc. We propose several simple optical setups, verify their accuracy, precision, and validate them in a user study.

**Keywords:** optometry; light-field display; computer-human interaction; refractive errors; visual accommodation.

## 1 Introduction

Measuring refractive properties of imaging systems is a common task in many applications ranging from industrial ones to optometry. The majority of these use sophisticated hardware to precisely estimate these aberrations. Emerging trends in high-resolution displays and interactive software in portable devices provide a new opportunity. In this paper, we explore novel estimation techniques based on interaction with a view-dependent display. Instead of an automated system, we put the user in the loop. This approach intriguingly is highly suitable for estimating refractive errors in the human eye. Although the majority of the paper deals with focusing abilities, aberrations, and range in a human eye, the techniques are also applicable to other optical systems. Our estimation method is not intended to replace the need for optometrists. Instead, the goal is to build a handy refraction screening tool, similar to modern electronic tools used to measure body temperature, blood oxygenation, or blood sugar that promote self-awareness.

We measure the refraction deviations using the dual of a Shack-Hartmann wavefront sensing approach by placing a microlens array or a pin-hole array over an LCD display. The user looks into this display at a very close range as shown in Figure 1. The key idea is that we can pre-warp position and angle of ray-beams from this display to counteract the effect of eye lens aberrations and create sharp aligned images on the retina. Via interactive software, the user aligns displayed patterns which in turn pre-warps this ray-space. The required pre-warp indicates the lens aberrations. In this



**Figure 1:** Can a person look at a portable display, click on a few buttons and recover his refractive fidelity? Our solution combines inexpensive optical elements, programmable display and interactive software components to create the equivalent of a parallax barrier display that interfaces with the human eye. Using this platform, we create a new range of interactivity for measuring several parameters of the human eye, such as refractive errors, focal range, and focusing speed.

paper, we explore the design parameters of our novel device as well as smart patterns to maximize its usability.

### 1.1 Contributions

We propose a novel device based on a view-dependent display to measure focusing abilities of an optical system. Our approach (called *NETRA*) exploits alignment rather than blur as an indicator of misfocus. The main contributions of our paper include:

- A co-design of optics and interactive software to create an effective, low-cost interface sensitive to refractive parameters of the human eye. We create an unusual optical configuration for a programmable display, which is the dual of a Shack-Hartmann system;
- An interactive method to create virtual objects at desired depths, adapted to eye aberrations, which allow one to indirectly measure refractive errors. We design patterns and GUI for providing optimal alignment and accommodation cues;
- Four designs for the optical probe;
- Validation via physical measurements and subject participation.

We believe ours is the only method that measures accommodation without a mechanically moving device or creating a virtual light source inside the eye, thus making it safer and more mobile. It trades mechanically moving parts for moving patterns on a digital screen, and replaces lasers or lights focusing into an eye with a method that relies on user feedback, allowing self-assessment. The technique goes beyond traditional lens aberration measurement and can also estimate range and speed of accommodation for eyes and cameras.

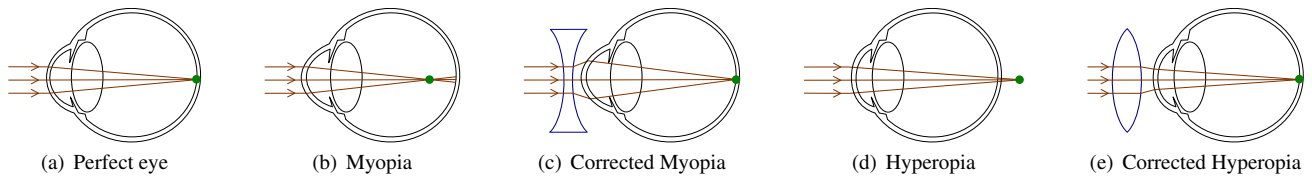


**Figure 2:** The human eye and some refractive disorders and corrections. (a) A perfect eye focuses parallel rays to a single point on the retina; (b) a myopic eye has an elongated eye ball or a bumped cornea, and parallel rays focus to a point before the retina; (c) myopia can be corrected with a diverging lens (negative diopters); (d) a hyperopic eye has a shallow eye ball or a flatter cornea, and parallel rays focus to a point after the retina; (e) hyperopia can be corrected with a converging lens (positive diopters).

## 1.2 Related Work

Many researchers have explored eye-related subjects in computer graphics. Barsky [2004] used wavefront data measured from a subject’s optical system to render images that simulate the subject’s vision. Deering [2005] presented a photon-accurate model of the cones in the human retina and used it to simulate the perception of displayed digital images. Sagar et al. [1994] created an anatomically detailed model of the eye for use in a surgical simulator. Pampalona et al. [2009] introduced a physiologically-based model for pupil light reflex. Lam and Baranoski [2006] presented a predictive light transport model for the human iris based on biophysical parameters. Several researchers have addressed the issue of realistic rendering of the human eye [Lefohn et al. 2003; Cui et al. 2004; Wecker et al. 2005; Makthal and Ross 2005; Ritschel et al. 2009]. We hope to add to this growing body of research.

**Displays:** Matching convergence and accommodation for displayed imagery is achieved using multi-focus displays [Akeley et al. 2004; Hoffman et al. 2005]. These could be used for our purposes to some extent. Liu and Hua [2009] have shown a liquid lens based solution to change the plane of focus inside a head mounted display (HMD). Rolland et al. [2000] showed a multi-planar volumetric display based on a stack of laminated planes that are selectively illuminated inside a HMD. Our approach achieves multi-focus without additional depth layers or mechanically moving lenses or lights. Thus, it can also be used to create novel multi-focus HMDs, although at significantly reduced spatial resolution.

**Ray Analysis:** Our work is inspired by recent work in shaping light rays using light-field techniques [Ng and Hanrahan 2006; Levoy et al. 2009] in computer graphics. Surprisingly, there has been little discussion of the connection between light fields and Shack-Hartmann technique in optics. Shack-Hartmann involves measuring the phase of the aberrated wavefront from a (distant) point source by placing a microlens array in front of a digital sensor. The displacement of the images under each lenslet indicates phase changes. The deviations in phase indicate turbulence or lens aberrations. Our method swaps the sensor for a digital display. Our optical setup is essentially an array of programmable Bokodes [Mohan et al. 2009], the combined effect of which produces a virtual image at an arbitrary distance.

## 2 The Human Eye and Refractive Errors

The human eye is a sophisticated imaging system capable of dynamically adjusting its refractive power to focus at a wide range of distances. The eye’s refractive power comes from two sources: the air-cornea interface, which is fixed and depends of the corneal shape, and the crystalline lens, which provides an additional and adjustable refractive power. During accommodation, the lens shape changes from more planar (when the eye is focusing at a far scene) to more spherical (when focusing at a near object). The eye is subject to refractive disorders as shown in Figure 2 due to imperfec-

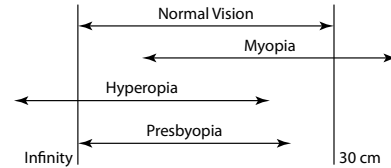


**Figure 3:** Range of focus for various eye refractive conditions. Myopia shifts the focal range closer, causing bad far sight. Hyperopia shifts the focal range farther (allowing focusing ability beyond infinity), causing bad near sight and lens fatigue since the crystalline lens does not relax even when looking at infinity. Presbyopia reduces the focal range and moves the nearest plane of focus away from the eye. Additionally, astigmatism produces radially non-symmetric focusing ranges for all of the above.

tions in the cornea, lens, or the shape of the eyeball.

Figure 3 illustrates the focal ranges for individuals with bad far sight (*myopia*), bad near sight (*hyperopia*), and with loss of accommodation power (*presbyopia*). These conditions are characterized by radially symmetric aberrations. More interesting conditions involve astigmatism and higher order aberrations. Refractive correction for myopia, hyperopia, and astigmatism can be achieved with the use of corrective lenses (Figure 2). The refractive power of a lens is expressed in *diopters*, a unit defined as the reciprocal of the lens’ focal length expressed in meters. For this paper, the reader can think of the eye as a camera with lens aberrations and limited focusing extent.

### 2.1 Comparison with Optometry

Perhaps the first indirect technique for detecting refractive errors in the human eye was the *Scheiner principle*, from 1619. Light enters the eye through two tiny holes on a disk placed next to the eye. This produces two spots on the retina of a myopic (or hyperopic) eye, which is easy to distinguish from the single spot formed on a perfect eye. This basic principle is applied in most modern solutions for measuring refractive errors, including ours. The art of prescribing correcting lenses is involved and often the prescription does not exactly match the estimated refractive errors. Our goal in this paper is not about estimating lens prescription, but to create a portable, inexpensive, and also fun tool for self-assessment of the eye’s focusing abilities. Techniques for estimating eye refractive errors can be classified as *subjective*, *objective*, or *hybrid*.

**Subjective Methods:** These techniques rely upon the user’s judgment of sharpness or blurriness of a test object, like the Snellen eye chart. Such charts are carefully calibrated, and are designed to be observed from standard distances, under controlled illumination, and contain standardized symbols (*optotypes*). Alone, these charts only provide very rough and arbitrary measures of acuity.

**Objective Methods:** These methods require a mechanically moving lens or light setup to check ray vergence. *Wavefront-sensing*

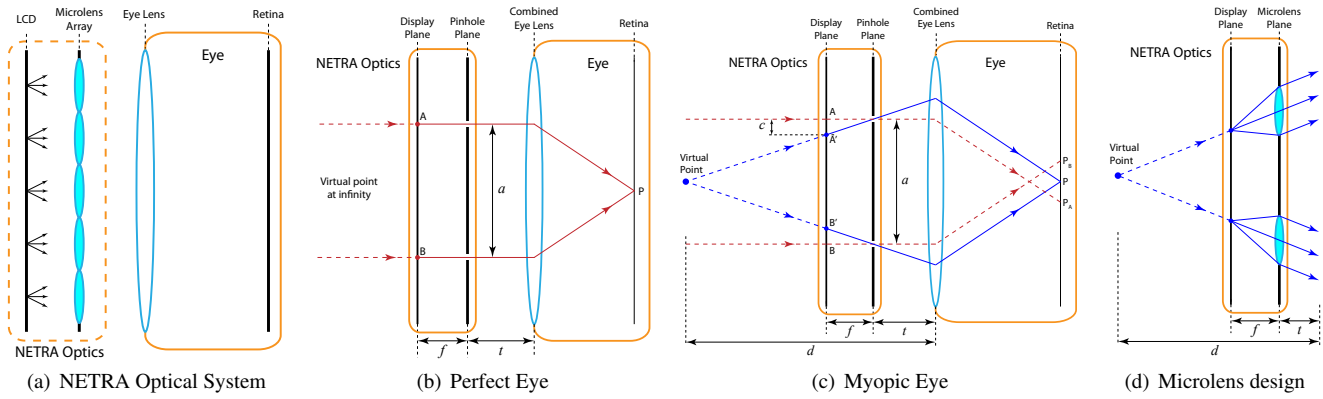


**Figure 4:** NETRA optical setup: (a) a microlens array placed over a high-resolution display is held right next to the eye. For simplicity, we use a single lens to represent the combined refractive power of the cornea and the crystalline. (b) The NETRA optical system using a pinhole array. A perfect eye converges parallel rays onto a point on the retina. (c) A myopic eye converges a set of parallel rays before the retina (red arrows). By shifting points  $A$  and  $B$  to  $A'$  and  $B'$ , respectively, the resulting rays focus on the retina at point  $P$  (blue arrows). The amount of shift required to move  $A$  to  $A'$  allows us to compute refractive error. (d) Microlens design of the system improves the light throughput.

techniques measure the total amount of aberration in the images formed on the subject’s retina and, therefore, accounts for the eye’s entire optical path [Liang et al. 1994]. The Shack-Hartmann technique for wavefront sensing analyzes the distortions observed in a known light pattern reflected on the human retina. *Tscherning aberrometry* [Tscherning 1894] uses a collimated beam of laser light that passes through a regular array of (hundreds of) holes and should focus to a single point on the human retina when the subject is focusing at infinity. The deviations of the light paths allow one to estimate the aberrations. A fundus camera is used to capture the image of these distorted spots. *Laser Raytracing* [Navarro and Losada 1997] is similar, but it replaces the mask with a moving narrow laser beam that scans the pupil. The fundus camera captures one retinal image at a time and estimates the light path inside the eye. The aberration is computed by the deviations of these light paths. These devices directly focus bright light into the eye and hence require specialized equipment, operators, and mechanical motion. They do not allow for easy self-evaluation.

**Hybrid Methods:** Currently, the most common way used by doctors to prescribe corrective lenses consists of two steps. First, an estimate of the patient’s prescription is obtained automatically with an auto-refractometer. Then, this estimate is subjectively verified and refined using lenses and an eye chart. *Spatially Resolved Refractometry* [Webb et al. 1992] measures the eye aberrations based on the subjective judgment of the patient. A cross pattern is projected (normally via a laser) onto the subject’s retina. Several light beams (about 40) are then projected, one at a time, through different points on the pupil. For each beam, the user moves its projection to the center of the cross pattern. The difference between the initial angle of a beam and the adjusted angle gives the wavefront error.

Our system *combines both estimation and verification in a single step and employs an alignment task instead of a blur test*. This contrasts with the most common practice in optometry today. The ability to project virtual patterns at different distances from the viewer allows us to measure the range and speed of accommodation.

**Portable Devices:** Several commercial products (such as the Nikon Retinomax), and research prototypes of portable and handheld optometers and auto-refractometers exist. The Focometer [Berger et al. 1993] and OptiOpia [OptiOpia] target developing countries, while a handheld Scheiner-principle optometer by Cushman [1993] targets field use for transient accommodation deficiencies. Unlike these, our system does not contain moving parts, and retrofits any high-resolution display (such as those used on mobile phones).

**Limitations:** Since our solution relies on subjective feedback, it cannot be used by individuals who cannot reliably perform the user-required tasks, such as very young children. The accuracy of the measurements is limited by the focal length of the microlens array (or pinhole mask) and by the dot pitch of the underlying display. Accuracy, however, is expected to improve as technology evolves.

### 3 Creating Programmable Depth Perception

We describe the intuition behind our approach using the concept of a virtual point source created by the new display. Figure 4(a) shows the basic optical setup of our system for self-evaluation of visual accommodation. We place a microlens array or a pin-hole array over a controllable high-resolution display. The viewer holds this setup next to the eye being tested. The image formed on the viewer’s retina depends on the refractive properties of the tested eye. Using a simple interaction scheme, the user modifies the displayed pattern until the perceived image closely matches a specified result. Based on this interaction, we estimate the viewer’s refractive conditions, such as myopia, hyperopia, and astigmatism.

Figure 4(b) shows a simplified ray diagram for our system with two pinholes in flatland. In practice, we use 8 pinholes or 8 microlens (positioned on the eight neighbors of a cell centered at a  $3 \times 3$  grid). As we illuminate one point directly under each pinhole (points  $A$  and  $B$ ), two parallel rays enter the eye simulating a virtual point at infinity. An eye that can focus at infinity converges these rays, which meet at a single spot  $P$  on the retina. A *myopic* eye (bad far-sight), however, is unable to focus at infinity, and converges these incoming rays before the retina, producing two distinct spots ( $P_A$  and  $P_B$ ), as shown in Figure 4(c).

Changing the position of point  $A$  (or  $B$ ) changes the vergence of the rays produced by the pinholes. For instance, moving points  $A$  and  $B$  closer to each other on the display plane, causes the corresponding rays to diverge, progressively moving the virtual point closer to the viewer. Likewise, moving these points apart, causes the associated rays to converge, moving the virtual point away from the observer. For a myopic eye, as we move points  $A$  and  $B$  closer, we can make the two imaged spots overlap on the retina at  $P$  (Figure 4(c)). The amount of shift applied to  $A$  and  $B$  allows us to compute the refractive error in the viewer’s eye. The case for hyperopia (bad near-sight) is similar: as we move points  $A$  and  $B$  further apart on the display plane, we cause the resulting rays to converge, creating a virtual point “beyond infinity”.

The amount of shift  $c$  required to create a virtual source at a distance  $d$  from the eye is:

$$c = f(a/2)/(d - t), \quad (1)$$

where  $t$  is the distance from the pinhole array to the eye,  $a$  is the spacing between the pinholes, and  $f$  is the distance between the pinhole array and the display plane.  $f$  is also the focal length of the lenses for the microlens array based setup. Using a programmable LCD, we can arbitrarily vary the distance between the virtual scene point and the eye without any moving parts. This is equivalent to varying the power of a lens placed in front of the eye. From Equation 1, the power of a diverging lens required to fix myopia is given (in diopters) by  $D = (1/d) = 1000/(f(a/2)/c+t)$ , where all distances are in  $mm$ . Positive values for  $c$  and  $D$  represent myopia, while negative values represent hyperopia.

**Alignment instead of blur:** Unlike a real point, our virtual point projects a discontinuous set of rays into the eye. The number of rays arriving from the virtual point is limited to the number of pinholes. This produces a discontinuous circle of confusion for a point that is out of focus. In the case of two pinholes, we obtain two points on the retina. This subtle difference allows us to *convert a blur estimation problem into an easier alignment problem*.

In the lens-based setup, we place a microlens array at a distance from the display equal to its focal length. Instead of a single ray coming from each pinhole in one direction, we get a bundle of parallel rays, as shown in Figure 4(d). This introduces a **focus ambiguity**: the eye can focus (or *accommodate*) either at the virtual point at a distance  $d$ , or at infinity to focus the parallel bundle of rays on the retina. Forced focus at infinity is ideal for measuring myopia, while accurate measurement of hyperopia requires accommodation to completely relax the eyes. In Section 5, we describe techniques for making one focus cue stronger than the other by varying the displayed patterns.

**Crosstalk between microlenses** or pinholes may occur when the pattern meant for one lenslet is visible through an adjacent lenslet. This produces additional images of the overlapping patterns on the viewer’s retina, which might be confusing. We address this problem by skipping every alternate lenslet. In a pinhole-based setup, we use jittered pinholes and patterns as discussed in Section 5. **Chromatic aberration** in the eye and microlens may produce virtual points at different depths, making the use of colored patterns tricky. However, we use color patterns in one of our prototypes (Figure 8) to increase the effective display resolution with reasonable success. The **pupil size** limits the maximum spacing between lenslets (distance  $a$  in Figure 4), which affects the achievable range of corrective power. Also, the granularity of the microlens array affects the accuracy for the cylindrical axis (in the case of astigmatism).

The diopter **resolution** of our setup is limited by the size of the cone cells of the eye (effectively the pixel size of the retina),  $p_e \sim 4\mu m$ , and eye’s focal length,  $f_e \sim 17mm$ . We assume that the human user can resolve misalignments of a single pixel or cone cell. If the pixel size of our display is  $p_d$ , the smallest shift  $c = p_d$ , the maximum resolution of our setup (in diopters) from Equation 1 and assuming  $t \sim 0$ , is

$$D_{min} = 2000 \max\left(\frac{p_d}{fa}, \frac{p_e}{f_e a}\right). \quad (2)$$

With a pin-hole spacing,  $a = 3mm$ , this comes to 0.15 diopters at the upper bound set by  $p_e$ . This is further reduced by diffraction in the eye and the NETRA optics.

The analogy of generation of a virtual point by the NETRA optics is intuitive and works well with spherical lenses, but is inadequate for non-radially symmetric or higher-order aberrations.

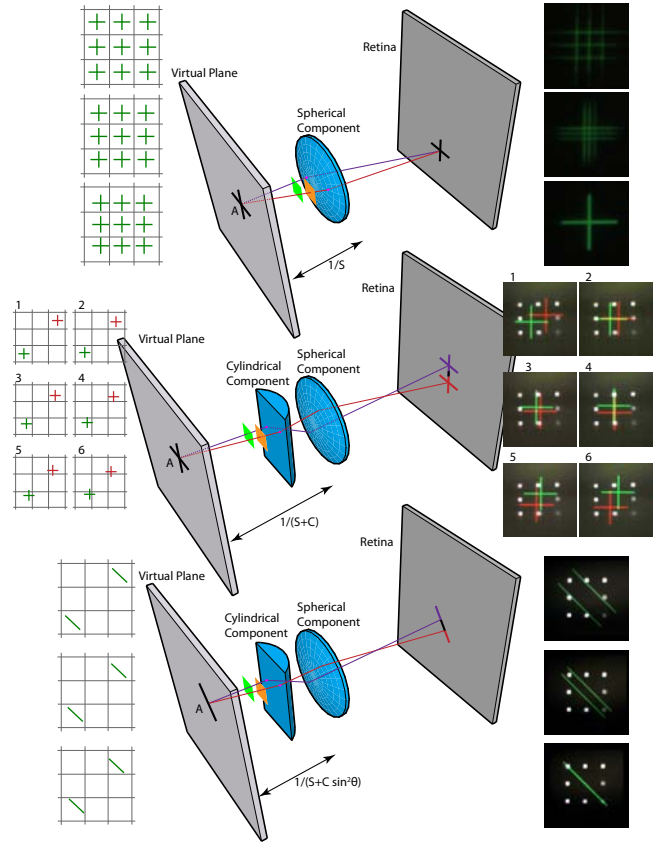


**Figure 5:** Alignment challenges in the context of astigmatism aberrations. Small images on the left show the patterns displayed on the screen as the viewer moves them closer to each other. Each cell of the grid represents the display under a pinhole/lenslet. Images on the right show how the viewer sees the respective image on left. (Top) For an eye with only spherical aberrations, we measure the spherical power  $S$  by displaying a cross pattern under the green and orange lenslets. The user then moves the patterns until they align on the retina. This alignment happens when the virtual cross  $A$  is at distance  $1/S$  from the lens. (Middle) Unfortunately, the creation of virtual points in the focal plane of the sphero-cylindrical lens at  $1/(S + C)$  does not assist with alignment in presence of cylindrical aberrations. Unlike the spherical case, the cross sign centers do not necessarily meet if we simply move them toward or away from the center. (Bottom) Our solution involves moving line segments oriented perpendicular to the line joining the two lenslets. The spacing at which these lines are perceived by the user as overlapping gives the power along the corresponding meridian.

## 4 Measuring Focal Range and Astigmatism

We measure **myopia** using the alignment technique described in Section 3. The viewer looks through the microlens array and sees multiple partially overlapping patterns (one from each lenslet - Figure 5). The viewer proceeds with a 1D search and tries to align the patterns by shifting them under the lenslets (either moving them closer or moving them apart). The spacing between the patterns (on the LCD) when they appear aligned (as seen by the user through our probe) gives a measure of myopia. Section 5 discusses some of the patterns that we use, and Figure 5(right) shows a sequence of images seen by a camera with simulated myopia. Throughout this process, the viewer’s eye is focused as close to infinity as it can get (completely relaxed state) due to the bundle of parallel rays arriving from each lenslet.

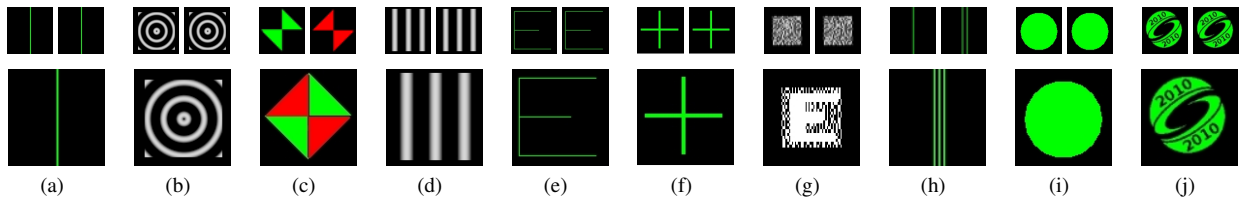


**Figure 6:** Patterns evaluated by the users sorted by the standard deviation (diopters) of the differences among 18 alignments for each. The standard deviation is shown in parenthesis next to the pattern names. Smaller numbers means better repeatability. Top: pairs of shapes used for alignment. Although most shapes in a pair are replicas of each other, some are not. Bottom: pattern obtained after the corresponding shapes are perfectly aligned. (a) Pair of single lines (0.10); (b) Concentric sinusoidal rings (0.13); (c) Crosshair (0.14); (d) Sinusoidal bars (0.16); (e) Letter E (0.17); (f) Cross (0.24); (g) VCS (0.26); (h) 2 lines  $\times$  1 line (0.28); (i) Circle (0.28); (j) SIGGRAPH logo (0.34).

For measuring **hyperopia**, we move the virtual point away from the eye causing it to accommodate until the lens is completely relaxed, but the image is still sharply focused. Moving the virtual point any farther results in multiple overlapping images. The distance at which the eye is no longer able to focus on the pattern gives a measure of the degree of hyperopia.

**Astigmatism** is a common refractive error due to irregular shape of the cornea and/or the eye lens. The analogy of moving a virtual point, although useful as a tool for understanding, does not extend to astigmatism. Here we need to look at how the generalized ray-space is transformed outside and inside the eye. An astigmatic eye is often modeled as a toric (sphero-cylindrical) patch, and its refractive power  $P(\theta)$  along a meridian with direction  $\theta$  is characterized as

$$P(\theta) = S + C \sin^2(\alpha - \theta), \quad (3)$$

where  $S$  is the eye's spherical power,  $C$  is its cylindrical power, and  $\alpha$  is the angle of the cylinder axis [Thibos et al. 1997]. It follows that  $\min(P(\theta)) = S$ , and  $\max(P(\theta)) = S + C$ .

Unfortunately aligning any general pattern (such as a cross) is not easy in presence of astigmatism due to cylindrical aberrations as shown in Figure 5(middle). Unlike the spherical case, moving two dots along the radial direction produces a spiral in their observed positions, and they may never overlap. A single virtual point maps to two different image points. Lines aligned with the cylindrical axis (vertical axis in Figure 5) are collinear but lines at any other orientation do not become collinear. Since the astigmatism axis is not known a-priori, it is challenging to design patterns and their movement for optimal alignment strategies. Allowing 2D perturbations to align two points works but the process is slow, tedious, and error prone [Webb et al. 1992].

Our solution involves exposing two lenslets at a time oriented at angle  $\theta$  (Figure 5(bottom)). We notice that only a line segment placed at orientation  $(\theta + \pi/2)$  will become collinear when the virtual image is created in the front focal plane at a distance  $1/(S + C \sin^2(\alpha - \theta))$  from the lens. The diopter at this meridian is calculated by computing the number of steps required while moving these two parallel line segments perpendicular to each other. By evaluating the eye's refractive errors along  $\theta \in [0, \pi)$ , we obtain the values for the eye's  $S$ ,  $C$ , and  $\alpha$  parameters. In practice, we collect a small number of such measurements (up to 8) along equally-spaced meridians, and use them to find an optimal (in the least squares sense) estimate of the eye's parameters.

For measuring **accommodation range**, in addition to testing the far focusing distance, we also test the close focusing distance by moving the virtual point closer until the eye stops focusing on it. This also gives a measure of **presbyopia** (bad near sight due to old age), where the lens has a reduced accommodation range. We adopt a two step process where we first measure for astigmatism. We

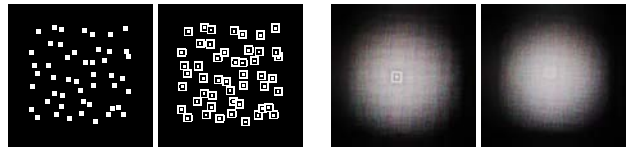


**Figure 7:** (Left) Jittered pinhole pattern (h) and corresponding display mask (p) for 0 diopters; (right) a normal eye sees a distinct pattern (g) in the middle, while a myopic eye sees a blurred image.

then project symmetric accommodation patterns along the cylindrical axis for testing accommodation range.

## 5 Choosing the Best Patterns

Our system provides two distinct focus cues for the viewer - one at infinity and another at a finite depth. The ability to switch between the two provides greater flexibility in measuring refractive errors and accommodation range.

**Patterns for alignment:** Most subjective methods for estimating eye refractive errors rely on blur due to mis-focus. Inspired by the Scheiner principle, we convert the task of blur assessment into a perceptually easier one of pattern alignment. However, instead of using a distant scene or cycloplegic eye drops to suspend accommodation, we rely on the bundle of parallel rays coming from each lenslet to fix eye focus at (for a perfect eye) or close to (for a myopic eye) infinity. Also, we use the two extreme lenslets to produce a disjoint blur and discourage accommodation.

We asked subjects to align the pairs of patterns shown in Figure 6 while observing them through our probe. Each pair of patterns was aligned three times by each subject. The subjects were constrained to move the patterns only horizontally (1D translation). For subjects requiring refractive correction, the experiment was performed without the use of corrective lenses. For each subject, we recorded the time required to align each pattern, as well as the error (measured in diopters) between repetitions. **Visual cryptography** (VCS) patterns [Naor and Shamir 1994] rely on perception to decode information (Figure 6(g)). We place the two secret shares under separate lenslets, and the hidden pattern is revealed when they perfectly align. Unfortunately these patterns do not offer any indication of how far the viewer is from the alignment until it is achieved. While the average alignment time was approximately the same for all patterns (about 10 seconds), the pair of line segments produced the most consistent results in terms of repeatability (Figure 6(a)). We adopted the line segments as the pattern for measuring myopia, hyperopia and astigmatism.

**Patterns for accommodation:** We force the eye to focus at the virtual point produced by our optical setup by using a smooth sinusoidal pattern (Figures 6(b) and 6(d)). To encourage accommodation, we use identical patterns under the lenslets. Such patterns are

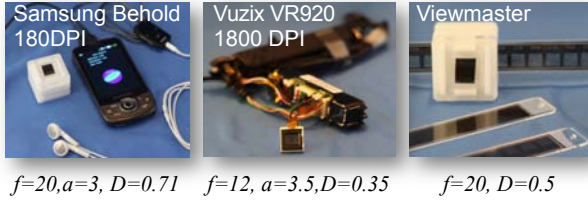


**Figure 8:** Three of our prototypes: (left) cell phone, (center) high-resolution display, (right) View-Master.

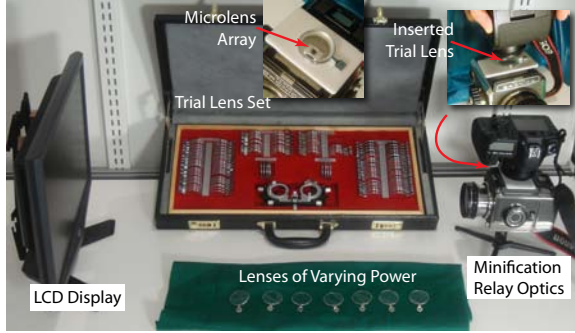


**Figure 9:** Evaluation setup and trial lens set.

useful for measuring accommodation range and speed, and presbyopia. We use the 1D sinusoid (Figure 6(d)) for our range test and symmetrically project it along the axis of the cylindrical power.

**Hybrid patterns:** These patterns allow for both accommodation and alignment. Smooth transitions in the pattern encourage accommodation, while sharp parts allow the user to easily judge when the images are misaligned, or out of focus. An example is a combination of the sinusoidal pattern with the line pattern. We use this pattern to test whether the user is focusing at infinity, and for measuring accommodation range. The sinusoidal pattern is displayed under several lenslets, and the lines are displayed only under the extreme lenslets; the lines overlap when the image is in focus, and split when the patterns misalign.

**Jittered patterns:** For the View-Master setup (Figure 8(right)), we relax the constraint of regularly spaced pinholes. Instead, we jitter each pinhole by a small amount. We also correspondingly jitter the pattern behind each pinhole in the display mask as shown in Figure 7. The jittered pattern converts the crosstalk between pinholes into random noise. This is useful when pinhole spacing is small (more light throughput) or mask to pinhole distance is large (increased power resolution) and structured crosstalk may confuse the viewer. Due to the irregular arrangement, these patterns are harder to use with microlens arrays.

Given a desired pattern,  $g$ , and a jittered pin-hole array,  $h$ , placed at distance  $f$  from pattern  $p$ , we obtain the pattern  $p$  by convolution,  $p = h \otimes g$ . The eye when focused at infinity integrates all the parallel rays into a single spot, and the parallel ray intensity in angular direction  $\beta$  is given by  $h(x)p(x - f\beta)$ . Thus, the formed eye image is given by  $I(\beta) = \sum_x (h(x)p(x - f\beta)) = h \star p$ , where  $\star$  implies cross-correlation. Thus,  $I = h \star h \otimes g$ . It is clear that to present image  $g$  to a human eye, we must use a jittered pinhole pattern  $h$ , whose autocorrelation is a delta function.

## 6 Prototypes and Evaluation

**Evaluation Setup:** For ease of set up and execution, we did most of our experiments on an LCD screen with minimizing relay optics (Figure 9). This setup uses a 24" Dell 2407WFP LCD display

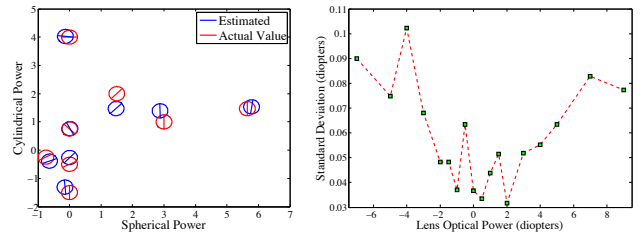


**Figure 10:** Estimating lens parameters. Left: Parameters estimated with our system and the actual values for several sphero-cylindrical lenses. The circles are centered at the corresponding spherical ( $S$ ) and cylindrical ( $C$ ) values. The line segments inside the circles are the cylindrical axes. Blue represents estimated values, and red represents actual values. Right: Standard deviation in diopters of a six round estimation of the power for a set of spherical lenses in the  $[-7, 9]$  diopters range.

play ( $1920 \times 1200$  pixels) coupled with an optical minification system (factor of  $1/35.8$ ), and an array of  $20 \times 20$  500-microns lenslets with focal length  $12.5\text{mm}$  (Edmund Optics part number NT64-479). The minification system creates a virtual display of 3,320 DPI on the focal plane of the micro lenses, which is equivalent to a  $7.5\mu\text{m}$  pixel-pitch display. As per Equation 1, we have  $a = 3.5\text{mm}$ , and  $c = 0.0075 \times \text{number of displaced pixels}$ . An eyepiece guarantees that  $t = 15\text{mm}$ , giving approximately  $\pm 0.16$  diopters per displaced pixel on the LCD. As per Equation 2, this setup is close to being limited by size of the cone cells in the eye.

Besides the evaluation setup just described, we also explore different designs shown in Figure 8 that span across size, and interface, but mainly screen resolution (pixels per inch). For the **cell phone setups**, we used a Samsung Behold II, which has a display with 180 DPI (or 540 DPI with three color channels in 1D), and the Google Nexus One phone, which has a display with 250 DPI (or 750 DPI with three color channels in 1D). Using a pinhole mask with  $3\text{mm}$  hole pitch and a distance  $f = 20\text{mm}$ , these prototypes provide approximately 0.71 diopter and 0.4 diopter per displaced pixel, respectively. The pinhole array pattern is a regular  $3 \times 3$  grid where each squared pinhole has a width of  $0.5\text{mm}$ . We also used a Vuzix iWear VR 920 **head mounted display** (1806 DPI) and a 500-microns lenslets with focal length  $12.5\text{mm}$  (Edmund Optics part number NT64-479), which results in  $\pm 0.35$  diopters per displaced pixel when  $a = 3.5\text{mm}$ . The **View-Master setup** uses jittered patterns and a translating mask instead of an LCD display.

### 6.1 Controlled Evaluation

We evaluate the accuracy of our prototype using a camera focused at infinity, with an additional lens of known power from an optometry trial lens set in front of it. We manually shift the patterns seen through a live-view on a PC connected to the camera and find the shift required for optimal alignment. We compare the power of the additional lens with the computed refractive power.

Figure 10(left) compares our estimated results with the actual lens parameters for a set of sphero-cylindrical lenses. The circles are centered at the corresponding spherical ( $S$ ) and cylindrical ( $C$ ) power values. The line segments inside the circles are the cylindrical axes. For this experiment, the average absolute errors for the spherical power, cylindrical power, and cylindrical axis were 0.09 diopters (standard deviation  $\sigma = 0.056$  diopters), 0.23 diopters ( $\sigma = 0.19$  diopters), and 8.43 degrees ( $\sigma = 6.16$  degrees), respectively. Figure 10(right) shows the absolute errors in the measurements performed with our system on six rounds of estimating the power for a set of spherical lenses in the  $[-7, 9]$  diopters range.

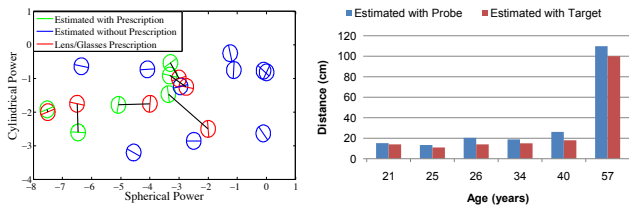


**Figure 11:** User evaluation. Left: Refractive errors estimated for several subjects using our system. Green represents estimated values for subjects with known prescription, which are shown in red and connect to the corresponding estimates by a line segment. Blue shows measurements made with our system for patients with unknown prescriptions. Right: Closest focal distance (in cm) estimated for a group of subjects of different ages estimated using both our probe (blue) and a reading target (red).

## 6.2 User Evaluation

We evaluate our system with a group of 13 volunteers (ages 21 to 57). For each subject, we estimate their spherical ( $S$ ) and cylindrical ( $C$ ) refractive errors, as well as the corresponding cylindrical axis ( $\alpha$ ). Figure 11(left) shows the estimated refractive error for each volunteer. For subjects with known prescriptions, we show the results for both eyes. For the others, we only show the results for one eye. The small line segments inside the circles represent the orientations of the cylinder axis. The estimated values using our system are reasonably close to the actual prescriptions. The average absolute errors from the known prescriptions were under 0.5 diopter ( $\sigma = 0.2$ ) for both cylindrical and spherical powers. The average absolute error of our estimates of the cylindrical axis was under 6 degrees. Optometrists typically prescribe in multiples of 0.25 diopter, and 10 degrees axis. The differences between our estimates and the actual prescriptions possibly result from imperfect calibration and other physical limitations of our prototype, inadequate directions to the volunteers on how to use our system, and tiredness during the experiment. Also, optometrists sometimes deviate slightly from objective measurements based on subjective factors such as patients' comfort and age in deciding the final prescription.

Deviations of the actual spacing between the eyeball and the probe from the assumed value of  $t = 15\text{mm}$  can introduce a small variation in the recovered power. Higher powers are more sensitive to these variations in  $t$ . For instance, a deviation in  $t$  of  $\pm 10\text{mm}$  results in an absolute variation of zero for a perfect eye focused at infinity, as small as 0.1 diopter for an eye with power  $\pm 3$  diopters, and about 0.5 diopter for an eye with power  $\pm 7$  diopters. This is not very critical though; as shown in Figure 11, even people with power as high as  $-8$  diopters obtained accurate results with our prototype.

**Eye Accommodation Range:** We measure the closest focal distance of a viewer using our system, and compare this with ground truth measurements. According to our experiments, sinusoidal patterns are the most appropriate for inducing accommodation changes with our system, and we project a 1D sinusoid along the axis of the cylindrical power for those with astigmatism. These observations seem to be supported by findings in the ophthalmology literature [Day et al. 2009]. We used our system to project a sinusoidal pattern at various distances from the viewers, who were asked to focus at the pattern. Figure 11(right) shows the closest distances at which a group of subjects with various ages (21 to 57) could focus at, and the corresponding distances estimated using a reading target. During our user evaluation, 2 of the 13 test subjects experienced difficulties in changing accommodation with our current patterns. Further research is required to identify intelligent patterns that can induce accommodation changes in those individuals.



**Figure 12:** Our probe is used to test refocusing speed (left) and focus range (center). Closest distance at which different camera-lens configurations can focus at (right). The blue bars are estimated distances with our probe. The red bars are estimates obtained using an optical bench.

## 7 Digital Camera Applications

Our device has a time-dimension and is also useful for estimating speed of accommodation. Our approach is suitable to detect healthy conditions of the ciliary muscles, temporary tiredness, or intoxication. We show a virtual pattern at some depth and in the next frame change it to a different depth. A young subject takes approximately 350ms to re-accommodate. While we did not evaluate these applications, we used our probe to check the speed of focusing of a consumer video camera. We show a virtual object at infinity and, in the very next frame, show the virtual object at 20 cm (Figure 12(left)).

We use our probe to evaluate *focusing range and speed* for various digital cameras. We identify the closest distance at which a camera can focus using an optical bench (Figure 12(center)). We use our probe to create a virtual pattern at a certain distance from the camera and then move the pattern closer. At each distance, we check whether the camera-lens configuration can still focus at the virtual pattern. We record the closest distance (Figure 12(right)).

## 8 Discussion and Conclusion

**Conclusions:** We have presented an interactive technique based on a novel near-eye optical probe and high-resolution display. We believe this is the only wavefront aberration estimation method without moving parts or retinal illumination. Substituting mechanically moving parts with moving patterns on a digital screen requires careful consideration of the impact of asymmetric aberrations, such as astigmatism, in 3D. We designed 2D patterns and their movement that mimic virtual sources and allow intuitive manipulation by the users. Our adaptive two-step process allows us to estimate the relaxed state aberration via alignment as well as the focusing range via accommodation cues. Our unusual configuration leads us to explore a variety of patterns and we have shown that a signal processing approach provides greater freedom to create view-masks and patterns. We can also estimate focusing range and speed, which is rarely available in other devices.

**Future Work:** We see several future directions of research. Computer graphics techniques can greatly benefit from a multi-focus display. Although, the spatial resolution is diminished in our display, a dynamic parallax barrier created with two LCD screens can trade frame rate for spatial resolution by sequentially exposing different pin-holes. If the spatial and angular resolution is sufficiently high, we can create displays (such as an alarm clock) with optical correction in-built. A person with refractive error can read the clock without fiddling for eyeglasses. Our current approach emphasized accommodation, but convergence measurement is another direction of future exploration. Our display is 4D plus time. We experimented with color and time-based patterns (blinking), but none of them produced any qualitatively different results. This, however, remains an interesting area of research. Diagnosing other diseases such as cataract, retinal stray light and amblyopia (also known as lazy eye) is fruitful future work. Finally, we were pleas-

antly surprised to achieve 0.71 diopter accuracy on a mobile phone display. Mobile-phone-based distribution and our View-Master inspired probe have a lot of potential in developing regions of the world.

**Reactions from optometrists:** We have been working closely with ophthalmology researchers and practicing optometrists who are encouraged by the quality of our results. We are working towards conducting field trials in USA, Africa and India in collaboration with various NGOs and healthcare providers.

The proposed device can be thought of as a thermometer for visual performance. Just as a thermometer measures the body temperature and does not prescribe medicines, we reinforce that our technique provides a measurement of the refractive error, and does not provide a complete prescription. Optometrists use several subjective factors in addition to the physical measurement to decide the final prescription. We propose the use of our technique as a self-awareness tool for use at home (to monitor refractive error over time), or in certain areas of developing countries where optometrists might not be available. We hope that our work will spur new research in using modern interactive displays, imaging techniques, and visually interactive procedures to create a new class of self-evaluation probes.

## Acknowledgments

Thanks to the volunteers who tested our device, Xiaoxi Wang and Andrew Song for prototype construction, Tiago Oliveira for the illustration, Tyler Hutchison for the voiceover, the entire Camera Culture group for their unrelenting support; and the reviewers for their valuable feedback. Dr. James Kobler (Mass. General Hospital), Dr. Joseph Ciolino (Mass. Eye and Ear Infirmary), and Dr. Fuensanta Vera Diaz (Schepens Eye Research Institute) provided valuable resources and insightful discussions about optometry and ophthalmology. Vitor and Manuel acknowledge CNPq-Brazil fellowships 142563/2008-0, 200763/2009-1, 200284/2009-6, 476954/2008-8. Ramesh Raskar is supported by an Alfred P. Sloan Research Fellowship.

## References

- AKELEY, K., WATT, S. J., GIRSHICK, A. R., AND BANKS, M. S. 2004. A stereo display prototype with multiple focal distances. In *SIGGRAPH 2004*, 804–813.
- BARSKY, B. A. 2004. Vision-realistic rendering: simulation of the scanned foveal image from wavefront data of human subjects. In *APGV 2004*, ACM, 73–81.
- BERGER, I., SPITZBERG, L., NNADOZIE, J., BAILEY, N., FEASTER, J., KUETHER, C., TRAN, M., AND SWANN, S. 1993. Testing the FOCOMETER - a new refractometer. *Optometry & Vision Science* 70, 4, 332–338.
- CUI, J., WANG, Y., HUANG, J., TAN, T., AND SUN, Z. 2004. An iris image synthesis method based on PCA and super-resolution. In *ICPR 2004*, IEEE Comp. Soc., 471–474.
- CUSHMAN, W. B., 1993. Small, simple and cost-effective scheiner-principle optometer with computer interface for automated assessment. US Patent 5223866.
- DAY, M., GRAY, L. S., SEIDEL, D., AND STRANG, N. C. 2009. The relationship between object spatial profile and accommodation microfluctuations in emmetropes and myopes. *Journal of Vision* 9 (10), 1–13.
- DEERING, M. F. 2005. A photon accurate model of the human eye. In *SIGGRAPH 2005*, vol. 24, 649–658.
- HOFFMAN, D. M., GIRSHICK, A. R., AKELEY, K., AND BANKS, M. S. 2005. Vergence–accommodation conflicts hinder visual performance and cause visual fatigue. *J. Vis.* 5, 10, 834–862.
- LAM, M. W. Y., AND BARANOSKI, G. V. G. 2006. A predictive light transport model for the human iris. In *EUROGRAPHICS 2006*, vol. 25, 359–368.
- LEFOHN, A., BUDGE, B., SHIRLEY, P., CARUSO, R., AND REINHARD, E. 2003. An ocularist’s approach to human iris synthesis. *IEEE Computer Graphics and Applications* 23, 6, 70–75.
- LEVOY, M., ZHANG, Z., AND MCDOWALL, I. 2009. Recording and controlling the 4D light field in a microscope. *Journal of Microscopy* 235, 2, 144–162.
- LIANG, J., GRIMM, B., GOELZ, S., AND BILLE, J. 1994. Objective measurement of wave aberrations of the human eye with the use of a Hartmann-Shack sensor. *JOSA A* 11, 1949–1957.
- LIU, S., AND HUA, H. 2009. Time-multiplexed dual-focal plane head-mounted display with a liquid lens. *Optics Letters* 34, 11, 1642–1644.
- MAKTHAL, S., AND ROSS, A. 2005. Synthesis of iris images using markov random fields. In *EUSIPCO 2005*.
- MOHAN, A., WOO, G., HIURA, S., SMITHWICK, Q., AND RASKAR, R. 2009. Bokode: Imperceptible visual tags for camera based interaction from a distance. In *SIGGRAPH 2009*.
- NAOR, M., AND SHAMIR, A. 1994. Visual cryptography. In *EUROCRYPT 1994*, 1–12.
- NAVARRO, R., AND LOSADA, M. 1997. Aberrations and relative efficiency of light pencils in the living human eye. *Optometry & Vision Science* 74, 540–547.
- NG, R., AND HANRAHAN, P. 2006. Digital correction of lens aberrations in light field photography. In *SPIE International Optical Design Conference*, vol. 6342.
- OptiOpia. <http://www.optiopia.com/>.
- PAMPLONA, V. F., OLIVEIRA, M. M., AND BARANOSKI, G. 2009. Photorealistic models for pupil light reflex and iridal pattern deformation. *Transactions on Graphics* 28(4), 106.
- RITSCHER, T., IHRKE, M., FRISVAD, J. R., COPPENS, J., MYSZKOWSKI, K., AND SEIDEL, H.-P. 2009. Temporal glare: Real-time dynamic simulation of the scattering in the human eye. *EUROGRAPHICS* 28, 3, 183–192.
- ROLLAND, J. P., KRUEGER, M. W., AND GOON, A. 2000. Multifocal planes head-mounted displays. *Applied Optics* 39, 19, 3209–3215.
- SAGAR, M. A., BULLIVANT, D., MALLINSON, G. D., AND HUNTER, P. J. 1994. A virtual environment and model of the eye for surgical simulation. In *SIGGRAPH 1994*, 205–212.
- THIBOS, L., WHEELER, W., AND HORNER, D. 1997. Power vectors: An application of fourier analysis to the description and statistical analysis of refractive error. *Optometry and Vision Science* 74, 6, 367–375.
- TSCHERNING, M. 1894. Die monochromatischen aberrationen des menschlichen auges. *Z. Psychol. Physiol. Sinn.* 6, 456–471.
- WEBB, R., PENNEY, C., AND THOMPSON, K. 1992. Measurement of ocular wavefrontdistortion with a spatially resolved refractometer. *Applied Optics* 31, 3678–3686.
- WECKER, L., SAMAVATI, F., AND GAVRILOVA, M. 2005. Iris synthesis: a reverse subdivision application. In *GRAPHITE 2005*, 121–125.